Journal of Hazardous Materials 196 (2011) 342–349

Contents lists available at SciVerse ScienceDirect

Journal of Hazardous Materials

journal homepage: www.elsevier.com/locate/jhazmat

Preparation of nanocrystalline $Fe_{3-x}La_xO_4$ ferrite and their adsorption capability for Congo red

Lixia Wang[a,b], Jianchen Li[a], Yingqi Wang[a], Lijun Zhao[a,*]

[a] Key Laboratory of Automobile Materials (Jilin University), Ministry of Education and School of Materials Science and Engineering, Jilin University, Changchun 130022, China
[b] School of Mechanical Science and Engineering, Northeast Petroleum University, Daqing 163318, China

ARTICLE INFO

Article history:
Received 2 June 2011
Received in revised form 8 September 2011
Accepted 9 September 2011
Available online 16 September 2011

Keywords:
La^{3+}-doped magnetite
Adsorption
Desorption
Wastewater treatment

ABSTRACT

This investigation was to increase the adsorption capacity of magnetite for Congo red (CR) by adulterating a small quantity of La^{3+} ions into it. The adsorption capability of nanocrystalline $Fe_{3-x}La_xO_4$ ($x = 0$, 0.01, 0.05, 0.10) ferrite to remove CR from aqueous solution was evaluated carefully. Compared with undoped magnetite, the adsorption values were increased from 37.4 to 79.1 mg g^{-1}. The experimental results prove that it is effectual to increase the adsorption capacity of magnetite by doped La^{3+} ions. Among the La^{3+}-doped magnetite, $Fe_{2.95}La_{0.05}O_4$ nanoparticles exhibit the highest saturation magnetization and the maximum adsorption capability. The desorption ability of La^{3+}-doped magnetite nanoparticles loaded by CR can reach 92% after the treatment of acetone. Furthermore, the $Fe_{3-x}La_xO_4$ nanoparticles exhibited a clearly ferromagnetic behavior under applied magnetic field, which allowed their high-efficient magnetic separation from wastewater. It is found that high magnetism facilitates to improve their adsorption capacity for the similar products.

1. Introduction

Dyes and pigments are widely used as the coloring agents. Colored organic effluent is produced in industries such as textiles, paper, plastics, leather, food and cosmetic, etc. The total dye consumption in textile industry worldwide is more than 10,000 tonnes/year and approximately 100 tonnes of dyes were discharged into waste streams by the textile industry every year [1]. It was reported that nearly 40,000 dyes and pigments are listed, which consist of more than 7000 different chemical structures [2]. Such colored effluent can affect photosynthetic processes of aquatic plants, reducing oxygen levels in water and, in severe cases, resulting in the suffocation of aquatic flora and fauna [3]. Dye effluents are the pollutants that contain chemicals that exhibit toxic effect towards microbial populations and can be toxic and carcinogenic to organisms and human beings.

Congo red (CR) (sodium salt of benzidinediazobis-1-naphthylamine-4-sulfonic acid) is metabolized to benzidine, a known human carcinogen and exposure to this dye can cause some allergic responses [4]. The treatment of contaminated CR in wastewater is difficult because the dye is generally present in sodium salt form giving it very good water solubility. Due to their chemical structures, dyes resist fade when exposed to light, water and many chemicals and therefore it was difficult to be decolorized once dyes were released into the aquatic environment. Synthetic dyes are difficult to biodegrade due to their complex aromatic structures, which provide them physico-chemical, thermal and optical stability. Also, the high stability of its structure makes it difficult to biodegrade and photodegrade [5]. To remove dyes and other colored contaminants from wastewaters, several physical, chemical, physico-chemical and biological methods (e.g., adsorption, coagulation-flocculation [6], biodegradation, ion-exchange, chemical oxidation [7], ozonation [8], nanofiltration [9], micellar enhanced ultrafiltration [10] and electrochemical methods have been developed. A number of adsorbents, such as activated carbon [11], orange peel [12], sawdust [13], montmorillonite [14], wheat bran and rice bran [15], and mesoporous Fe_2O_3 [16], have been used for the removal of CR from aqueous solutions. But the adsorption capacity of these adsorbents is not large. Adsorbent-grade activated carbon is cost-prohibitive and both regeneration and disposal of the used carbon are often very difficult [17]. Widespread application of some of these adsorbents is restricted due to high cost, difficult disposal and regeneration. One of the new developments for removing dyes from water or wastewater in recent years is to use ferrite as adsorbents [18,19]. However, there are still some practical problems to be solved, such as the incompatible relation between the magnetic properties and the sizes. As far as we know, the decrease of the particle size will increase the surface disorder of nanoparticles. Thus, the surface energy will increase with the decreasing particle sizes. However, the saturation magnetization of magnetic powders is decreased with the decrease of the particle sizes, which is a disadvantage

* Corresponding author. Tel.: +86 431 85095878; fax: +86 431 85095876.
E-mail address: lijunzhao@jlu.edu.cn (L. Zhao).

0304-3894/$ – see front matter © 2011 Elsevier B.V. All rights reserved.
doi:10.1016/j.jhazmat.2011.09.032

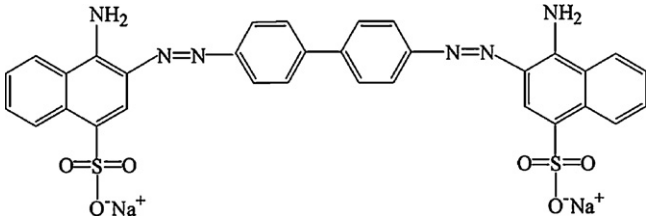

Scheme 1. Structure of Congo red molecule.

for the magnetic separation after the wastewater treatment. To solve this problem, in this contribution, the high surface activity is trying to be obtained by deforming the crystal structure which can be proved by the change of the lattice constant after substitution. Moreover, we have done an investigation on the relation between the adsorption activity and magnetic properties of $Fe_{3-x}La_xO_4$ nanoparticles. It is found that the higher magnetic properties facilitate to improve the adsorption capacity.

2. Materials and methods

2.1. Adsorbate

Congo red [CR, chemical formula = $C_{32}H_{22}N_6Na_2O_6S_2$, FW = 696.68, λ_{max} = 497 nm] is a benzidine-based anionic disazo dye, i.e., a dye with two azo groups. The structure is as illustrated in Scheme 1. An accurately weighed quantity of the dye was dissolved in double-distilled water to prepare stock solution (1 g L^{-1}).

2.2. Synthesis of nanocrystalline $Fe_{3-x}La_xO_4$ ferrite

In a typical experiment, $FeSO_4{\cdot}7H_2O$ and $LaCl_3{\cdot}7H_2O$ were dissolved in 20 mL of ethylene glycol (EG) by intensive stirring, accordingly a homogeneous solution was obtained, and then 1.5 g of NaOH was added to the solution at room temperature with simultaneous vigorous agitation. The mixtures were stirred vigorously for 30 min, and then sealed in a Teflon-lined stainless-steel autoclave and maintained at 200 °C for 8 h. After the completion of the reaction, the solid product was collected by magnetic filtration and washed several times with deionized water and absolute ethanol respectively. The final product was dried in a vacuum oven at 100 °C for 6 h. Black powders were obtained and characterized as $Fe_{3-x}La_xO_4$ (x = 0, 0.01, 0.05, 0.10). Detailed experimental parameters are listed in Table 1 (from S1 to S4). Furthermore, the experimental works were carried out in winter, so the room temperature was lower about 13 °C.

2.3. Characterization

The phases were identified by means of X-ray diffraction (XRD) with a Rigaku D/max 2500pc X-ray diffractometer with Cu Kα radiation (λ) 1.54156 (Å) at a scan rate of 0.02°/1(s), morphologies were characterized by a JEOL JSM-6700F field emission scanning electron microscopy (FESEM) operated at an acceleration voltage of 8.0 kV. Transmission electron microscope (TEM, Philips Tecnai 20, 200 kV), high-resolution transmission electron microscope (HRTEM, JEOL-3010, 300 kV) and Energy dispersive X-ray spectrum (EDX, Oxford Instruments INCA Energy TEM 200, 300 kV) were used to characterized the microstructure. The hysteresis loops were measured on a VSM-7300 vibrating sample magnetometer (VSM) (Lakeshore, USA) in room temperature. IR spectra of the samples were characterized using a FTIR spectrophotometer (NEXUS, 670) in KBr pellets. A UV–vis spectrophotometer was used for determination of CR concentration in the solutions.

Table 1
Summary of the experimental parameters.

Samples	$FeSO_4{\cdot}7H_2O$ (g)	$LaCl_3{\cdot}7H_2O$ (g)	NaOH (g)
S1 (Fe_3O_4)	0.8341 ± 0.0002	0.0000 ± 0.0002	1.5000 ± 0.0002
S2 ($Fe_{2.99}La_{0.01}O_4$)	0.8313 ± 0.0002	0.0037 ± 0.0002	1.5000 ± 0.0002
S3 ($Fe_{2.95}La_{0.05}O_4$)	0.8202 ± 0.0002	0.0185 ± 0.0002	1.5000 ± 0.0002
S4 ($Fe_{2.90}La_{0.10}O_4$)	0.8063 ± 0.0002	0.0371 ± 0.0002	1.5000 ± 0.0002

2.4. Adsorption experiments

The stock solution of CR (1 g L^{-1}) was prepared in deionized water and desired concentrations of the dye were obtained by diluting the same with water. The calibration curve of CR was prepared by measuring the absorbance of different predetermined concentrations of the samples at λ_{max} = 497 nm using UV–vis spectrophotometer (CR has a maximum absorbency at wavelength 497 nm on a UV–vis spectrophotometer). The amount of adsorbed CR (mg g^{-1}) was calculated based on a mass balance equation as given below:

$$q_e = \frac{(C_0 - C_e) \times V}{W} \quad (1)$$

where q_e is the equilibrium adsorption capacity per gram dry weight of the adsorbent, mg g^{-1}; C_0 is the initial concentration of CR in the solution, mg dm^{-3}; C_e is the final or equilibrium concentration of CR in the solution, mg dm^{-3}; V is the volume of the solution, dm^3; and W is the dry weight of the hydrogel beads, g.

Take one adsorption of CR for example. Standard solution with initial concentrations of 30 mg L^{-1} was prepared. Then, 15 mg of $Fe_{3-x}La_xO_4$ nanoparticles was added to 50 mL of the above solution under stirring. After a specified time, the solid and liquid were separated by magnet and UV–vis adsorption spectra was used to measure the CR concentration in the remaining solutions. A standard curve, which was used to convert absorbance data into concentrations for kinetic and equilibrium studies, was drawn to calculate the concentration of each experiment.

3. Results and discussion

3.1. Characterization of $Fe_{3-x}La_xO_4$

Fig. 1 shows the XRD patterns of S1 and S3. All the diffraction peaks in Fig. 1a can be indexed to the face-centered cubic structure of magnetite according to JCPDS card no. 19-0629, and the lattice constant of S1 is 8.40014 Å. The diffraction peaks of S3 show the same structure with S1, and no impurities can be detected from

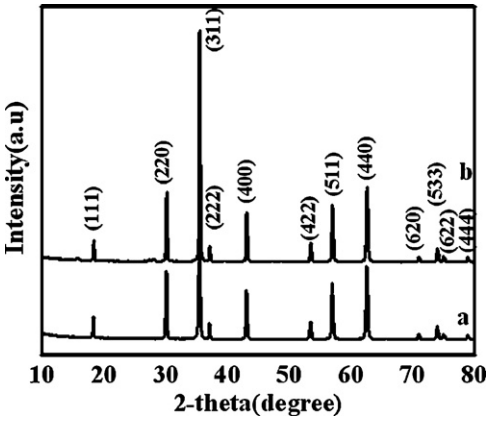

Fig. 1. XRD patterns of: (a) S1 and (b) S3.

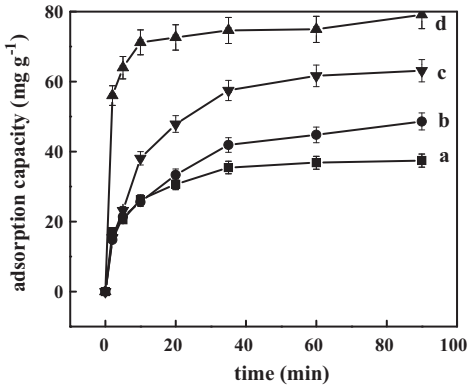

Fig. 2. Adsorption capacity of: (a) S1; (b) S2; (c) S4 and (d) S3. (Adsorption conditions for CR: 50 mL of 100 mg L^{-1} of dye, adsorbent dosage 0.015 g, natural pH, temperature: 13 °C.)

Fig. 1b. Furthermore, the lattice constant of S3 is 8.39244 Å. The incorporation of La ions may reside on the boundaries of the magnetite, which make the shortening of Fe–O bond length, therefore, the lattice constant of S3 is smaller than S1. Similar results have been reported in work done by Zhao and El-Bahy [20,21]. The strong and sharp peaks indicate that the S1 and S3 are well crystallized. By comparison of the lattice constants between S1 and S3, we can confirm that the crystal structure of magnetite was deformed little by the doping of La^{3+} ions.

3.2. Effect of La^{3+}-doped amount on the adsorption capacity of magnetite

After we ascertain the pure phase $Fe_{3-x}La_xO_4$ ferrites, a series adsorption experiments were carried out. The adsorption capacity of S1 to S4 for CR was shown in Fig. 2. Their adsorption values for CR are 37.4,48.6,79.1 and 63.1 mg g^{-1}, respectively. An exciting experimental result is obtained that the doping of La^{3+} ions favors increasing the adsorption capacity of magnetite for CR. Especially, S3 exhibits the maximum adsorption capacity. Furthermore, at the beginning of the contact time about 5 min, a rapid removal of CR was observed. After 90 min, the adsorption for CR almost reaches saturation.

In order to study the effect of morphologies or particle sizes of the $Fe_{3-x}La_xO_4$ on the adsorption capacity of CR in the aqueous solution, SEM photos were shown in Fig. 3a. S1 is composed by octahedral nanoparticles with edge length about 10–30 nm. Uniform nanoparticles with particle sizes around 20 nm are observed from Fig. 3b. However, irregular shapes and broad size distribution are appeared with the increasing doped contents of La ions for S3 and S4 (Fig. 3c and d). Their particle sizes are in the range of 60–200 nm and 80–300 nm, respectively. To our best knowledge, the adsorption capacity of nanopowders increased with the decrease of particle sizes (namely the increase of surface areas). However, in this experiment, it is found that the adsorption capacity could be improved by doped La^{3+} ions, without accompanying the decrease of the particle sizes.

Further insight into the nanostructure of samples was gained using TEM and HRTEM. Take S3 as example. Fig. 4a shows the TEM image of S3, which are in agreement with the above SEM findings. The HRTEM image (Fig. 4b) and the corresponding fast-Fourier-transform (FFT) pattern-which is framed in Fig. 4b with a square-is shown in Fig. 4c, it represents a face-centered cubic diffraction spots pattern. The clear lattice fringes can prove the high crystallinity of the as-prepared S3. Further, the dominantly exposed planes of S3 are {1 1 1}. The lattice spacing between two adjacent fringes we can observe is corresponding to the set of (1 1 1) planes with a lattice space of 0.5 nm. The lattice fringes are parallel throughout, which prove the single-crystalline nature of S3. Besides, EDX analysis (Fig. 4d) exhibited that S3 was essentially composed of Fe, La and O elements, indicating that La ions was introduced into the magnetite.

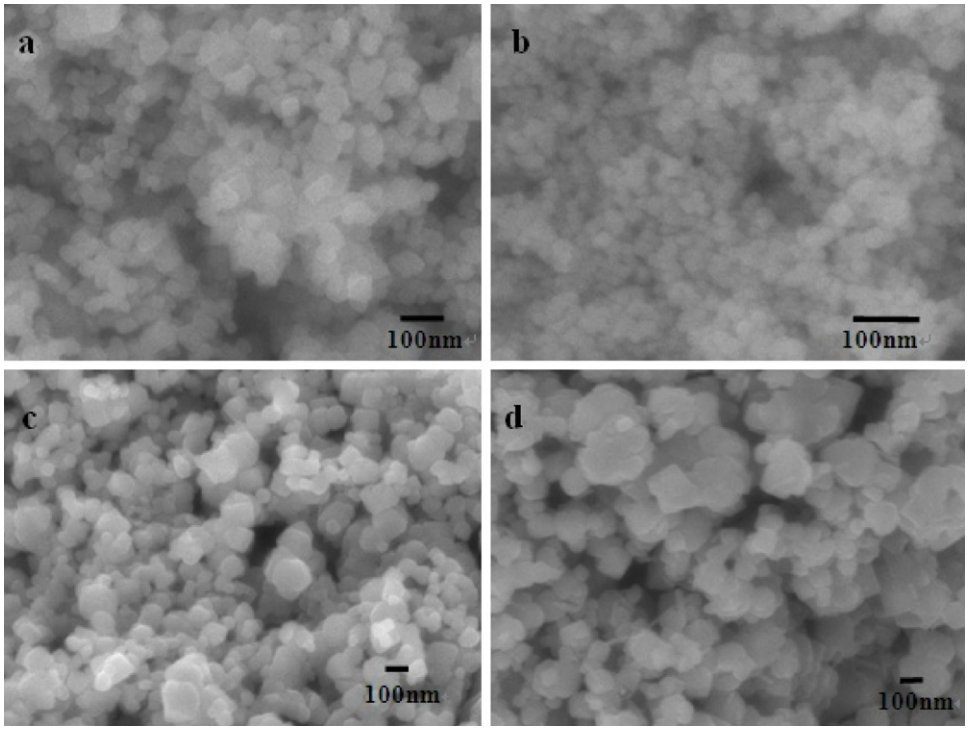

Fig. 3. SEM images of (a) S1, (b) S2, (c) S3 and (d) S4.

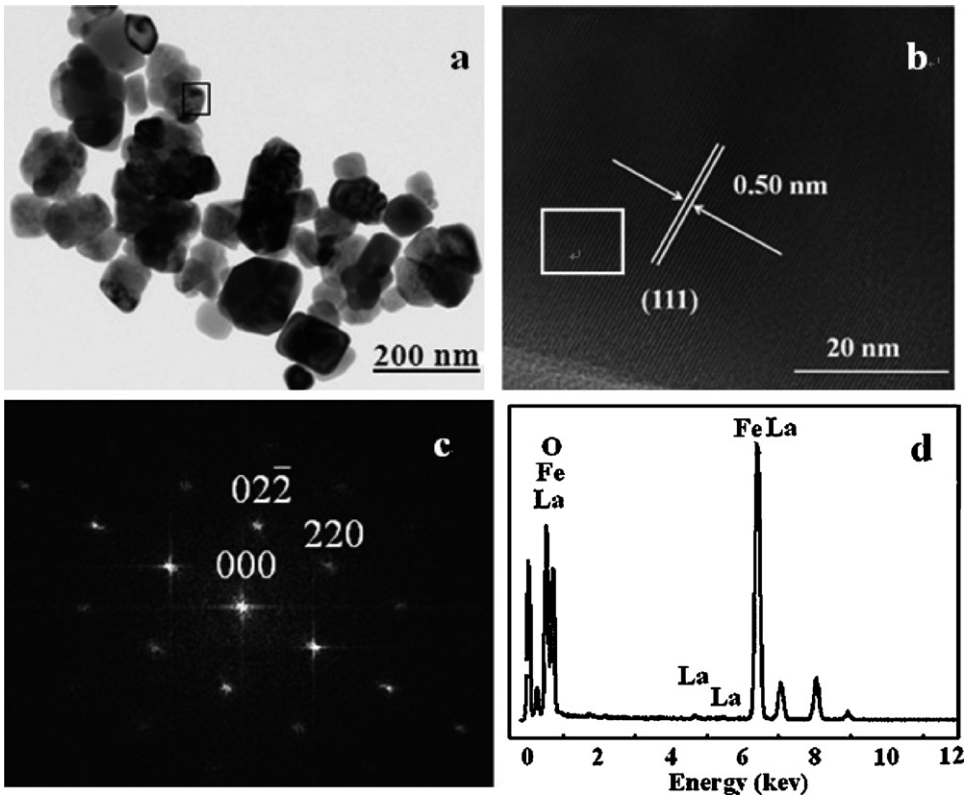

Fig. 4. (a) SEM image, (b) HRTEM image, (c) FFT pattern framed in (b), and (d) EDX pattern of S3.

3.3. Adsorption mechanism

By comparing the S1 with other samples, it is certain that the proper doped La^{3+} ions can effectively increase the adsorption capacity. Among the S2, S3 and S4, it can be concluded that the concentration of the doped La^{3+} ions and the particle sizes exhibit a combination influence on the adsorption capacity of magnetite. The proper doped amount and particle sizes lead to the maximum adsorption capacity of magnetite. The ionic radius (r) of La^{3+} is much larger than that of Fe^{3+} ($r_{La}{}^{3+} = 1.06$ Å, $r_{Fe}{}^{3+} = 0.64$ Å). Such a substitution makes the change of lattice constant. Compared S1 with S3, the lattice constant of S3 is smaller than that of S1. The lattice constant is corresponding to the distortion height of octahedral site ([MeO_6]) for magnetite with face-center cubic structure. The decrease of lattice constant makes the increase of distortion degree, hence, the magnetite substituted by La^{3+} ions is more unstable. Meanwhile, the dopant would lead the imperfect coordination and produce surface defects of magnetite. Finally, the unstable state might lead to the increase of surface energy. To decrease the surface energy of magnetite, it is prone to the adsorption of CR on its surface. Moreover, the structural mismatch caused by doped La^{3+} ions should change the surface charge of Fe_3O_4 [23], which may also conduce to the adsorption of CR on the surface based on the electrostatic adherence principle.

3.4. Effect of initial dye concentrations and contact time on adsorption

In order to know the effect of initial dye concentration and contact time on the removal of CR, four different concentrations (0.030, 0.050, 0.080, and 0.100 g L^{-1}) are selected to investigate the adsorption of CR on the surface of $Fe_{2.95}La_{0.05}O_4$. With the increase of initial CR concentrations from 0.030 to 0.100 g L^{-1}, the amount of CR removal was increased from 29.2 to 79.11 mg g^{-1} as shown in Fig. 5.

Very rapid adsorption is observed at previous 2–5 min, and thereafter a gradual increase occurs with increasing contact time up to 20–30 min depending on the initial dye concentration. Then, the adsorption keeps a weak increase during the following time. Therefore, the adsorption equilibrium almost happen at 40 min. Similar results have been reported for the adsorption of CR on calcium-rich fly ash in work done by Acemioğlu [24].

3.5. Adsorption isotherms

Analysis of adsorption isotherm is of fundamental importance to describe how adsorbate molecules interact with the adsorbent surface. To simulate the adsorption isotherm, two commonly used

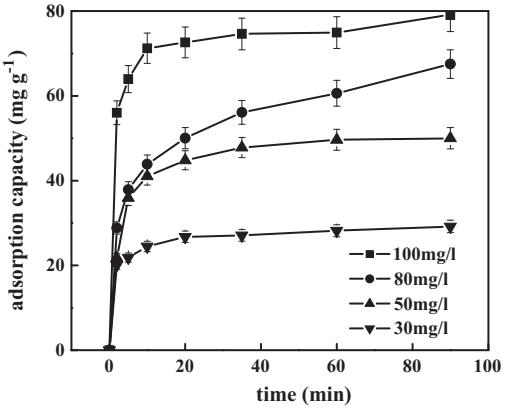

Fig. 5. Effect of initial dye concentration on CR removal from S3. (Conditions: 50 mL of CR, adsorbent dosage 0.015 g, natural pH, temperature: 13 °C.)

Table 2
Adsorption parameter obtained from adsorption isotherm for S3.

Freundich				Langmuir			
K_F	n	r_F^2	q_{max} (mg g^{-1})	K_L	r_L^2	R_L	C_0 (mg L^{-1})
9.8084 ± 0.0002	2.14 ± 0.01	0.9898 ± 0.0002	107.64 ± 0.01	0.0279 ± 0.002	0.9976 ± 0.0001	0.5444 ± 0.0002	30.0 ± 0.1
						0.4175 ± 0.0002	50.0 ± 0.1
						0.3094 ± 0.0002	80.0 ± 0.1
						0.2639 ± 0.0002	100.0 ± 0.1

models, the Freundlich [25] and Langmuir [26] isotherms, were selected to explicate dye–ferrite interaction.

The Freundlich adsorption isotherm can be expressed as:

$$\log\ q_e = \log K_F + \frac{1}{n}\log C_e \quad (2)$$

where K_F and n are the Freundlich adsorption isotherm constants, being indicative of the extent of the adsorption and the degree of nonlinearity between solution concentration and adsorption, respectively. K_F and $1/n$ values can be calculated from intercept and slope of the linear plot between log C_e and log q_e.

The Langmuir isotherm is expressed as:

$$\frac{1}{q_e} = \frac{1}{q_{max}} + \frac{1}{K_L q_{max}}\frac{1}{C_e} \quad (3)$$

where q_{max} is the maximum amount of adsorption with complete monolayer coverage on the adsorbent surface (mg g^{-1}), and K_L is the Langmuir constant related to the energy of adsorption (L mg^{-1}). The Langmuir constants K_L and q_{max} can be determined from the linear plot of $1/C_e$ versus $1/q_e$.

The essential characteristics of Langmuir isotherm can be expressed by a dimensionless constant called equilibrium parameter R_L that is defined by the following equation:

$$R_L = \frac{1}{(1 + K_L C_0)} \quad (4)$$

where K_L and C_0 are the same as defined before. The value of R_L calculated from the above expression. The nature of the adsorption process to be either unfavorable ($R_L > 1$), linear ($R_L = 1$), favorable ($0 < R_L < 1$) or irreversible ($R_L = 0$).

The Freundlich isotherm was employed to describe heterogeneous systems and reversible adsorption, which does not restrict to the monolayer formations. Unlike the Freundlich isotherm, the Langmuir isotherm is based on the assumption that a structure of adsorbent is homogeneous, where all sorption sites are identical and energetically equivalent.

Fig. 6 represents the plot of the experimental data based on Freundlich and Langmuir isotherms model, respectively. Table 2 shows the calculated values of Freundlich and Langmuir model's parameters. The comparison of correlation coefficients (r^2) of the linearized form of both equations indicates that the Langmuir model yields a better fit for the experimental equilibrium adsorption data than the Freundlich model. This suggests the monolayer coverage of the surface of S3 by CR molecules. The maximum adsorption capacity (q_{max}) of the S3 beads for CR was 107.64 mg g^{-1} (Table 2). Here, R_L-values obtained are listed in Table 2. All the R_L-values for the adsorption of CR onto S3 are in the range of 0.5444–0.2639, indicating that the adsorption process is favorable.

3.6. Adsorption kinetics

The adsorption kinetic models were applied to interpret the experimental data to determine the controlling mechanism of dye adsorptions from aqueous solution. Here, Pseudo-first-order, pseudo-second-order and the intraparticle diffusion model were used to test dynamical experimental data.

The pseudo-first order kinetic model of Lagergren [27] is given by:

$$\log(q_1 - q_t) = \log\ q_{1e} - \frac{K_1 t}{2.303} \quad (5)$$

where q_t is the amount of dye adsorbed per unit of adsorbent (mg g^{-1}) at time t, K_1 is the pseudo-first order rate constant (min^{-1}). The adsorption rate constant (K_1) were calculated from the plot of $\log(q_{1e} - q_t)$ against t.

Ho and McKay [28] presented the pseudo-second order kinetic as:

$$\frac{t}{q_t} = \frac{1}{K_2 q_{2e}^2} + \frac{t}{q_{2e}} \quad (6)$$

where K_2 is the pseudo-second order rate constant (g mg^{-1} min^{-1}). The initial adsorption rate, h (mg g^{-1} min^{-1}) at $t \to 0$ is defined as:

$$h = K_2 q_{2e}^2 \quad (7)$$

The h, q_{2e} and K_2 can be obtained by linear plot of t/q_t versus t.

Fig. 7 is the plots of the pseudo-first order and second order kinetics of CR adsorption on S3. The calculated kinetic parameters are given in Table 3.

The correlation coefficient for the pseudo-first-order model is relatively lower ($r_1^2 = 0.8527$), the calculated q_e value (q_{1e}) obtained

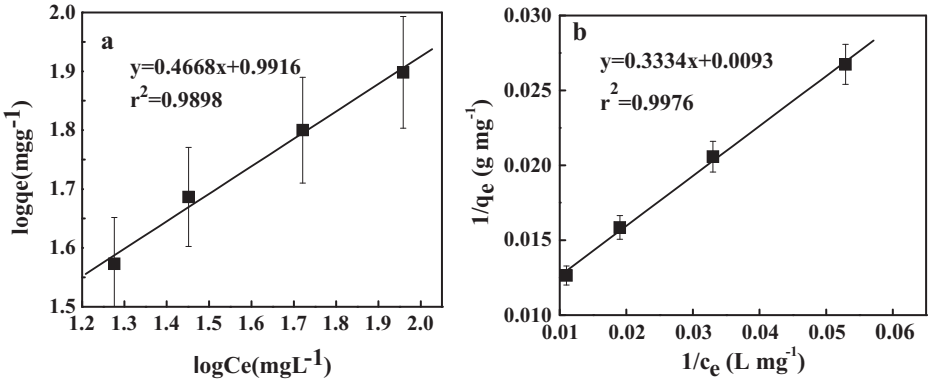

Fig. 6. Adsorption isotherms for adsorption of CR on S3 (15 mg of adsorbent) (a) Freundlich and (b) Langmuir.

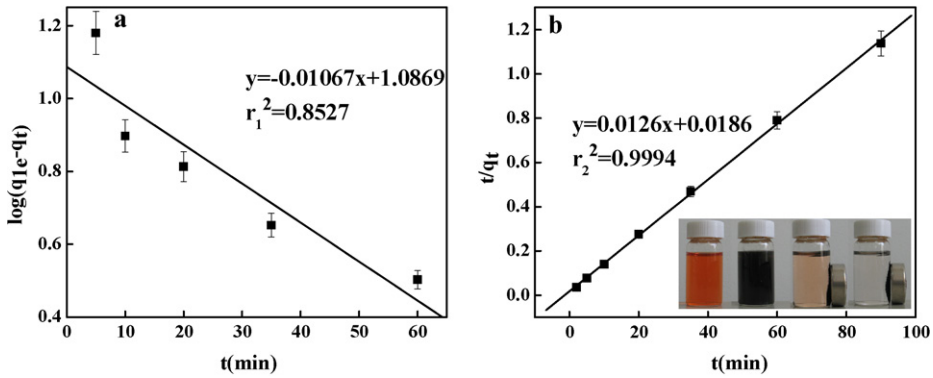

Fig. 7. Adsorption kinetic for adsorption of CR on S3 (15 mg of adsorbent, initial dye concentration 100 mg L^{-1}, natural pH, test-temperature: 13 °C) (a) pseudo-first order and (b) pseudo-second order. Inset in (b) in turn is CR solution, mixing with the magnetic absorbents and separation of the adsorbent from solution with a magnet after reaction (2) and 30 min, respectively.

Table 3
Adsorption parameters obtained from Fig. 5.

$q_{e,exp}$ (mg g^{-1})	Pseudo-first-order			Pseudo-second-order			
	K_1 (min^{-1})	q_{1e} (mg g^{-1})	r_1^2	K_2 (g mg^{-1} min^{-1})	q_{2e} (mg g^{-1})	h (mg g^{-1} min^{-1})	r_2^2
79.11 ± 0.01	0.0246 ± 0.0002	12.22 ± 0.01	0.8527 ± 0.0002	0.0085 ± 0.0002	79.43 ± 0.01	53.62 ± 0.01	0.9994 ± 0.0001

from this equation does not give reasonable value (Table 3), which is much lower than experimental data ($q_{e,exp}$). This result suggests that the adsorption process does not follow the pseudo-first-order kinetic model, which is similar to the result reported for adsorption of CR onto Australian clay materials [29]. On the contrary, the results present an ideal fit to the second order kinetic for adsorbent with the extremely high $r_2^2 = 0.9994$ (Fig. 7b). A good agreement with this adsorption model is confirmed by the similar values of calculated q_{2e} and the experimental ones for adsorbent. The best fit to the pseudo-second order kinetics indicates that the adsorption mechanism depends on the adsorbate and adsorbent. CR is an acidic dye with negative charge because of the existence of sulphonated group ($-SO_3^-$ Na^+). Here, the higher adsorption capacity of the CR for S3 is probably because of the dopant of La ions, which may increase the surface positive charges of magnetite, so we speculate that an electrostatic attraction may the main adsorption mechanism. Inset in Fig. 7b represented the photograph of adsorption and magnetic separation behavior. A light pink solution was observed after 2 min of adsorption. Further prolonging the adsorption time to 30 min, a colorless solution was gained. More importantly, simple and rapid separation of CR-loaded magnetite adsorbent from treated water can be achieved via an external magnetic field.

3.7. Desorption

Desorption is also a key role for the practical application of magnetic powders to water treatment. A facile desorption method and high-efficient desorption can facilitate to reduce cost, because the spent adsorbent and the CR can obtain recycling chance. Desorption process was conducted by mixing 5 mg of CR-loaded modified S3 with 30 mL of acetone solutions and shaking for different time. Fig. 8 is the desorption percentage with the time. The desorption efficiency calculated as Eq. (8) was 92%. Therefore, the CR could be desorbed from the loaded nanoparticles by acetone solutions.

$$\text{Desorption ratio } (\%) = \frac{\text{Amount of desorbed CR}}{\text{Amount of adsorbed CR}} \times 100 \quad (8)$$

FT-IR analysis was also performed to reveal the surface nature of S3, as shown in Fig. 9. The spectra display a broad band at 580 cm^{-1}, which is believed to be associated with the stretching vibrations of the tetrahedral groups (Fe^{3+}–O^{2-}) for S3. However, the band at 1050 cm^{-1} corresponding to C–N bond only appears in Fig. 9b, which discloses that CR was loaded on the surface of S3. This also serves as another evidence of physical adsorption because of in a physical adsorption at the mineral–water interface; an oxyanion

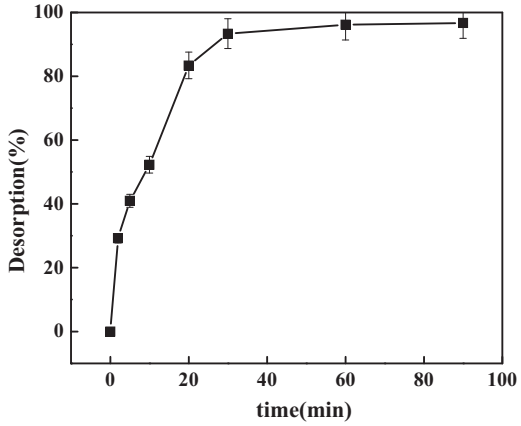

Fig. 8. Desorption ratio of loaded magnetite nanoparticles with time.

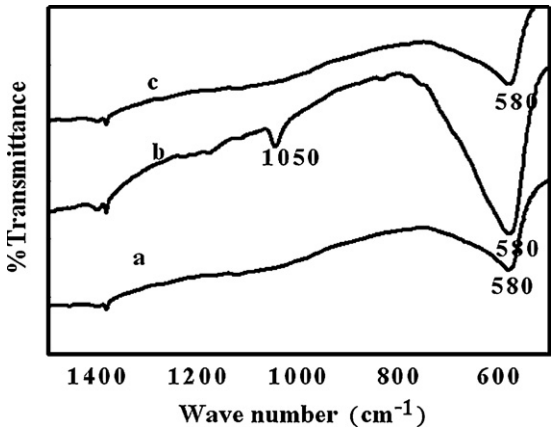

Fig. 9. FT-IR spectra of (a) as-prepared, (b) CR-absorbed and (c) CR-desorbed S3.

Table 4
Adsorption capacities of CR dye on various adsorbents.

Type of adsorbent	q_{max} (mg g^{-1})	Reference
Chitosan hydrogel beads impregnated with		
carbon nanotubesCS/CNT	450.40	[3]
Wheat bran	22.73	[15]
Rice bran	14.63	[15]
Maghemite nanoparticles	208.33	[16]
Cattail root	38.79	[29]
Sugar cane bagasse	4.43	[30]
Jute stick powder	35.70	[31]
Bentonite	19.90	[32]
Kaolin	5.60	[32]
Zeolite	4.30	[32]
Palm kernel seed coat	66.23	[33]
Activated red mud	7.08	[34]
Anilinepropylsilica xerogel	22.62	[35]
Marine alga	71.46	[36]
CTAB modified chitosan beads	352.50	[37]
CS/CTAB beads	373.29	[38]
$Fe_{2.95}La_{0.05}O_4$	107.64	Present study

will retain its hydration shell and will not form a direct chemical bond with the oxide surface [22]. Moreover, it is an evident proof that CR is removed sufficiently from the surface of S3 by acetone, because Fig. 9a and c exhibit the same FT-IR spectra.

3.8. Performance evaluation

The maximum adsorption capacity (q_{max}) for S3 nanoparticles to CR calculated from the Langmuir isotherm model is listed in Table 4 with literature values of q_{max} of other adsorbents for CR adsorption [3,15,16,29–38]. All of the adsorbents used for CR adsorption have considerably lower q_{max} values than S3 used in this study, except chitosan hydrogel beads impregnated with carbon nanotubes CS/CNT [3], maghemite nanoparticles [16] and CTAB modified chitosan beads [37,38]. However, the simplicity of the preparation method and magnetic separation of S3 nanoparticles makes them better adsorbent than the others for CR adsorption.

3.9. Magnetic properties

The magnetic properties of magnetic absorbents directly influence the callback efficiency. Hence, excellent magnetic performance is also a key role for the magnetic material as magnetic absorbent. Here, the magnetism of S1 to S4 is evaluated. It is exciting to find that the magnetic properties of magnetic absorbents do have influence on their adsorption ability.

The room-temperature hysteresis loops of S1 to S4 were shown in Fig. 10. Furthermore, the magnetic parameters of samples obtained from hysteresis loops were listed in Table 5. The test results show that the doped-La^{3+} ions make the *Ms* values of magnetite decreased to some extent. It must acknowledge that magnetite still keep the high *Ms* values after La^{3+} ions were doped into them, even if the lowest *Ms* value is 81.4 emu/g for S2. We amazingly find that the adsorption abilities of La^{3+}-doped magnetite are proportional to their *Ms* values and independent of their particle sizes. This is an important proof that excellent magnetism facilitates to increase the adsorption capacity for the similar magnetic products. Both the heavy-metal ions and organic matters show feeble paramagnetism or antiferromagnetism, so the magnetic powders which possess high *Ms* will be beneficial to the adsorption of heavy-metal ions and organic matters. Moreover, the magnetic materials with high *Ms* are help to the finally magnetic separation. Therefore, it is very meaningful to both keep the magnetic properties almost constant and increase the adsorption capacity.

Table 5
Magnetic parameters obtained from hysteresis loops.

Samples	*Ms* (emu/g)	*Mr* (emu/g)	*Hc* (Oe)
S1	90.5 ± 0.1	15.6 ± 0.1	156.6 ± 0.1
S2	81.4 ± 0.1	11.2 ± 0.1	116.5 ± 0.1
S3	86.2 ± 0.1	14.8 ± 0.1	115.9 ± 0.1
S4	82.2 ± 0.1	16.4 ± 0.1	105.9 ± 0.1

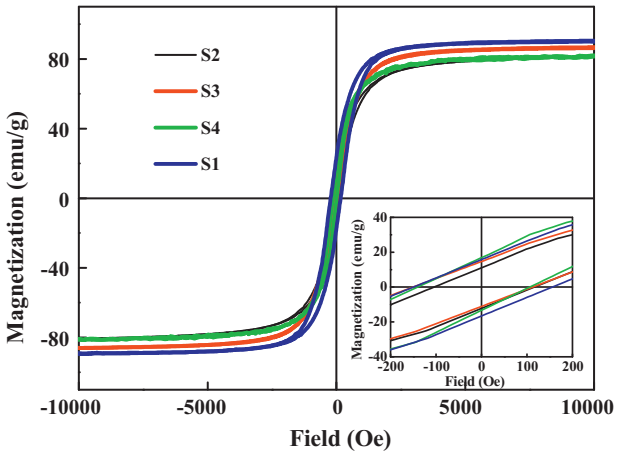

Fig. 10. Magnetization curve measured at room temperature for the $Fe_{3-x}La_xO_4$ ferrites.

4. Conclusions

$Fe_{3-x}La_xO_4$ (x = 0, 0.01, 0.05, 0.10) ferrite nanoparticles were successfully synthesized by a facile one-step solvothermal synthesis. Compared with the pure magnetite, La^{3+}-doped magnetite exhibit more excellent adsorption ability. Furthermore, among the La^{3+}-doped products, the sample ($Fe_{2.95}La_{0.05}O_4$) possessing the biggest *Ms* value owes the strongest adsorption capacity. The adsorption capacity of magnetite for CR is improved not by increasing the specific area but by deforming the crystal structure via doped- La^{3+} ions. By comparison with many other adsorbents, $Fe_{3-x}La_xO_4$ nanoparticles have higher adsorption capacities for CR. It would be a good method to increase adsorption efficiency of magnetite for the CR removal in a wastewater treatment process by doping La^{3+} ions. Analysis of adsorption isotherm shows that our adsorption experiment accord with Langmuir model. Again, adsorption kinetic model indicates that the adsorption mechanism depends on the adsorbate and adsorbent. In a word, the $Fe_{3-x}La_xO_4$ nanoparticles were a kind of excellent absorbent because of their high adsorption, desorption and recovery efficiency.

Acknowledgements

The financial supports from the Natural Science Foundation of Jilin Province (20101542) of China and the National Foundation of Doctoral Station (grant No. 20100061110019) are acknowledged.

References

[1] S.A. Saad, K.Md. Isa, R. Bahari, Chemically modified sugarcane bagasse as a potentially low-cost biosorbent for dye removal, Desalination 264 (2010) 123–128.
[2] A. Demirbas, Agricultural based activated carbon for the removal of dyes from aqueous solutions: a review, J. Hazard. Mater. 167 (2009) 1–9.
[3] S. Chatterjee, D.S. Lee, M.W. Lee, S.H. Wooa, Congo red adsorption from aqueous solutions by using chitosan hydrogel beads impregnated with nonionic or anionic surfactant, Bioresour. Technol. 101 (2010) 1800–1806.

[4] S. Chatterjee, M.W. Lee, S.H. Wooa, Adsorption of Congo red by chitosan hydrogel beads impregnated with carbon nanotubes, Bioresour. Technol. 100 (2009) 3862–3868.
[5] I.D. Mall, V.C. Srivastava, N.K. Agarwal, I.M. Mishra, Removal of Congo red from aqueous solution by bagasse fly ash and activated carbon: kinetic study and equilibrium isotherm analyses, Chemosphere 61 (2005) 492–501.
[6] M.L. Marechal, Y.M. Slokar, T. Taufer, Decolouration of chlorotriazine reactive azo dyes with H_2O_2/UV, Dyes Pigments 33 (1997) 181–298.
[7] M. Pollock, Neutralizing dye-housewastes with flue gases and decolorizing with fly ash, Am. Dyestuff Rep. 62 (1973) 21–23.
[8] G. Reynolds, N. Graham, R. Perry, R.G. Rice, Aqueous ozonation of pesticides: a review, Ozone Sci. Eng. 11 (1989) 339–382.
[9] S. Chakraborty, M.K. Purkait, S. Dasgupta, S. De, J.K. Basu, Nanofiltration of textile plant effluent for color removal and reduction in COD, Sep. Purif. Technol. 31 (2003) 141–151.
[10] M.K. Purkait, S. DasGupta, S. De, Removal of dye from wastewater using micellar-enhanced ultrafiltration and recovery of surfactant, Sep. Purif. Technol. 37 (2004) 81–92.
[11] M.K. Purkait, A. Maiti, S. DasGupta, S. De, Removal of Congo red using activated carbon and its regeneration, J. Hazard. Mater. 145 (2007) 287–295.
[12] M. Arami, N.Y. Limaee, N.M. Mahmoodi, N.S. Tabrizi, Removal of dyes from colored textile wastewater by orange peel adsorbent: equilibrium and kinetic studies, J. Colloid Interface Sci. 288 (2005) 371–376.
[13] R. Jain, S. Sikarwar, Removal of hazardous dye Congo red from waste material, J. Hazard. Mater. 152 (2008) 942–948.
[14] Z. Yermiyahu, I. Lapides, S. Yariv, Visible absorption spectroscopy study of the adsorption of Congo red by montmorillonite, Clay Miner. 38 (2003) 483–500.
[15] X.S. Wang, J.P. Chen, Biosorption of Congo red from aqueous solution using Wheat Bran and Rice Bran: batch studies, Sep. Sci. Technol. 44 (2009) 1452–1466.
[16] A. Afkhami, R. Moosavi, Adsorptive removal of Congo red, a carcinogenic textile dye, from aqueous solutions by maghemite nanoparticles, J. Hazard. Mater. 174 (2010) 398–403.
[17] X.S. Wang, J.P. Chen, Removal of the azo dye Congo red from aqueous solutions by the Marine Alga Porphyra yezoensis Ueda, Clean 37 (2009) 793–798.
[18] X.Y. Hou, J. Feng, X.H. Liu, Y.M. Ren, Z.J. Fan, M.L. Zhang, Magnetic and high rate adsorption properties of porous $Mn_{1-x}Zn_xFe_2O_4$ ($0 \leq x \leq 0.8$) adsorbents, J. Colloid Interface Sci. 353 (2011) 524–529.
[19] S.X. Zhang, H.Y. Niu, Y.Q. Cai, X. Zhao, Y.L. Shi, Arsenite and arsenate adsorption on coprecipitated bimetal oxide magnetic nanomaterials: $MnFe_2O_4$ and $CoFe_2O_4$, Chem. Eng. J. 158 (2010) 599–607.
[20] L.J. Zhao, H. Yang, L.X. Yu, W. Sun, Y.M. Cui, Y. Yan, S.H. Feng, Structure and magnetic properties of $Ni_{0.7}Mn_{0.3}Fe_2O_4$ nanoparticles doped with La_2O_3, Phys. Status Solidi 201 (2004) 3121–3128.
[21] Z.M. El-Bahy, A.A. Ismaila, R.M. Mohamed, Enhancement of titania by doping rare earth for photodegradation of organic dye (Direct Blue), J. Hazard. Mater. 166 (2009) 138–143.
[22] F.A. Petit, H. Debontride, M. Lenglet, G. Juhel, D. Verchere, Contribution of spectrometric methods to the study of the constituents of chromating layers, Appl. Spectrosc. 49 (1995) 207–210.
[23] Y.N. Shen, H.L. Zhao, X.T. Liu, N.S. Xu, Preparation and electrical properties of Ca-doped $La_2NiO_{4+\delta}$ cathode materials for IT-SOFC, Phys. Chem. Chem. Phys. 12 (2010) 15124–15131.
[24] B. Acemioğlu, Adsorption of Congo red from aqueous solution onto calcium-rich fly ash, J. Colloid Interface Sci. 274 (2004) 371–379.
[25] H.M.F. Freundlich, Uber die adsorption in losungen, Z. Phys. Chem. 57 (1906) 385–470.
[26] I. Langmuir, The adsorption of gases on plane surfaces of glass, mica and platinum, J. Am. Chem. Soc. 40 (1918) 1361–1403.
[27] S. Lagergren, About the theory of so-called adsorption of soluble substances, Kungliga Svenska Vetenskapsakademiens, Handlingar 24 (1898) 1–39.
[28] Y.S. Ho, G. McKay, Pseudo-second order model for sorption processes, Process Biochem. 34 (1999) 451–465.
[29] V. Vimonsesa, S. Lei, B. Jin, C.W.K. Chow, C. Saint, Kinetic study and equilibrium isotherm analysis of Congo red adsorption by clay materials, Chem. Eng. J. 148 (2009) 354–364.
[30] N.A. Oladoja, A.K. Akinlabi, Congo red biosoption on palm kernel seed coat, Ind. Eng. Chem. Res. 48 (2009) 6188–6196.
[31] A.S. Raymundo, R. Zanarotto, M. Belisário, M.G. Pereira, J.N. Ribeiro1, A.V.F.N. Ribeiro, Evaluation of sugar-cane bagasse as bioadsorbent in the textile wastewater treatment contaminated with carcinogenic Congo red dye, Braz. Arch. Biol. Technol. 53 (2010) 931–938.
[32] G.C. Panda1, S.K. Das1, A.K. Guha, Jute stick powder as a potential biomass for the removal of Congo red and rhodamine B from their aqueous solution, J. Hazard. Mater. 164 (2009) 374–379.
[33] T. Tuutijarvi, J. Lu, M. Sillanpaa, G. Chen, As (V) adsorption on maghemite nanoparticles, J. Hazard. Mater. 166 (2009) 1415–1420.
[34] Z. Hu, H. Chen, F. Ji, S. Yuan, Removal of Congo red from aqueous solution by cattail root, J. Hazard. Mater. 173 (2010) 292–297.
[35] A. Tor, Y. Cengeloglu, Removal of Congo red from aqueous solution by adsorption onto acid activated red mud, J. Hazard. Mater. 138 (2006) 409–415.
[36] L. Wang, A.Q. Wang, Adsorption characteristics of Congo red onto the chitosan/montmorillonite nanocomposite, J. Hazard. Mater. 147 (2007) 979–985.
[37] L. Wang, A.Q. Wang, Removal of Congo red from aqueous solution using a chitosan/organomontmorillonite nanocomposite, J. Chem. Technol. Biotechnol. 82 (2007) 711–720.
[38] S. Chatterjee, M.W. Lee, S.H. Woo, Influence of impregnation of chitosan beads with cetyl trimethyl ammonium bromide on their structure and adsorption of Congo red from aqueous solutions, Chem. Eng. J. 155 (2009) 254–259.